Supplementary Information:

Multichannel cavity optomechanics for all-optical amplification of radio frequency signals

Huan Li[1], Yu Chen[1], Jong Noh[1], Semere Tadesse[1], Mo Li[11]

[1]*Department of Electrical and Computer Engineering, University of Minnesota, Minneapolis, MN 55455, USA*

Supplementary Figures

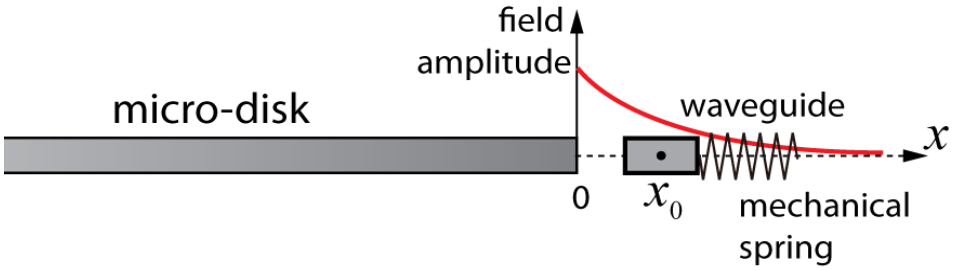

Supplementary Figure S1. Coordinate system defined for our device used in the theoretical calculation included in the supplementary methods. The red line marks the decaying field amplitude outside the micro-disk.

[1]Corresponding author: moli@umn.edu

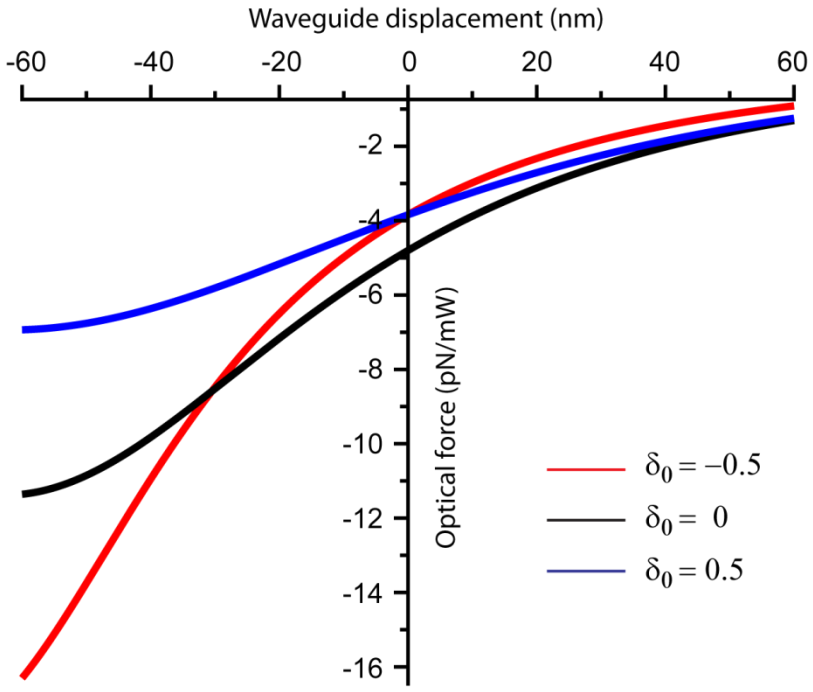

Supplementary Figure S2. Calculated optical force (normalized by the input power at the control channel) versus the signal waveguide displacement for different normalized static detuning values, showing strong nonlinearity.

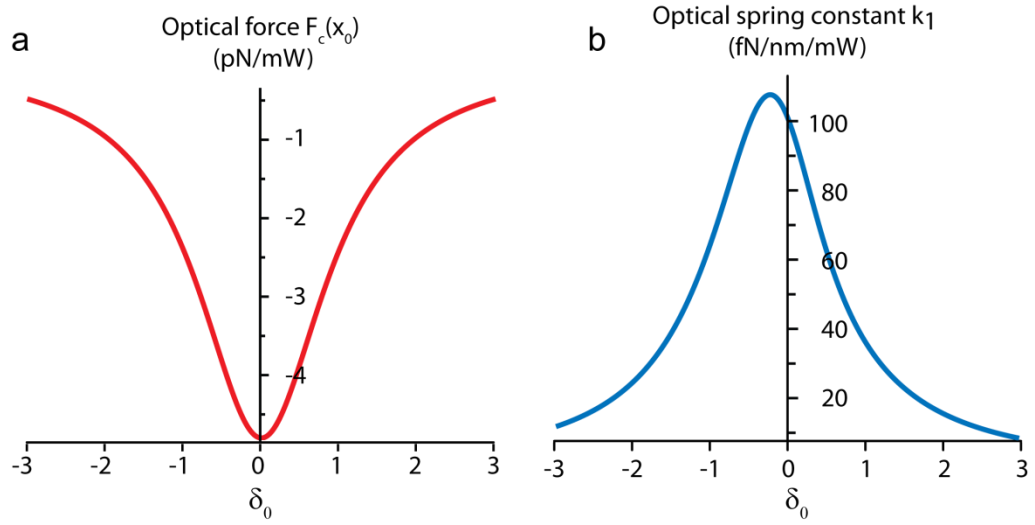

Supplementary Figure S3. Calculated static optical force $F_c\ x_0$ (**a**) and optical spring constant k_1 (**b**) of our device, normalized to the control channel power, as a function of normalized static detuning.

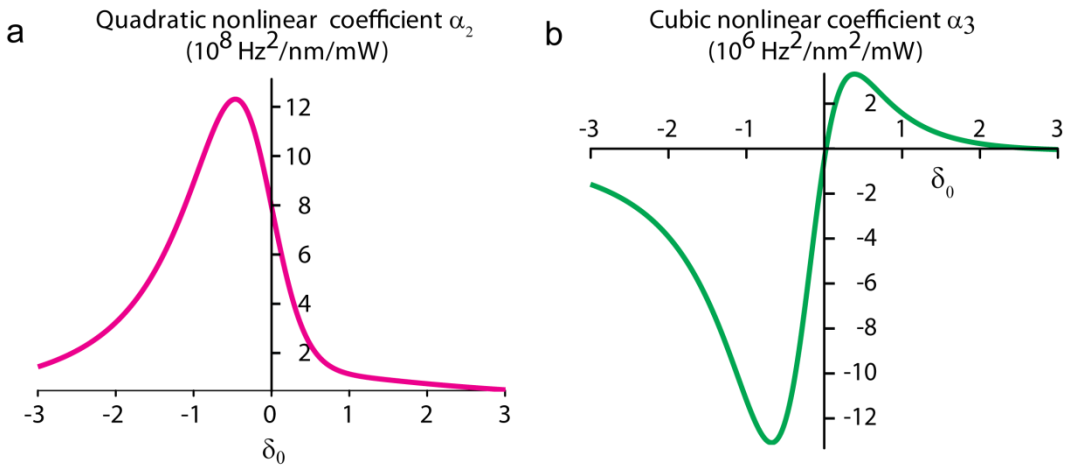

Supplementary Figure S4. Calculated quadratic (**a**) and cubic (**b**) nonlinear coefficients (α_2 and α_3) of our device, normalized to the control channel power, as a function of normalized static detuning.

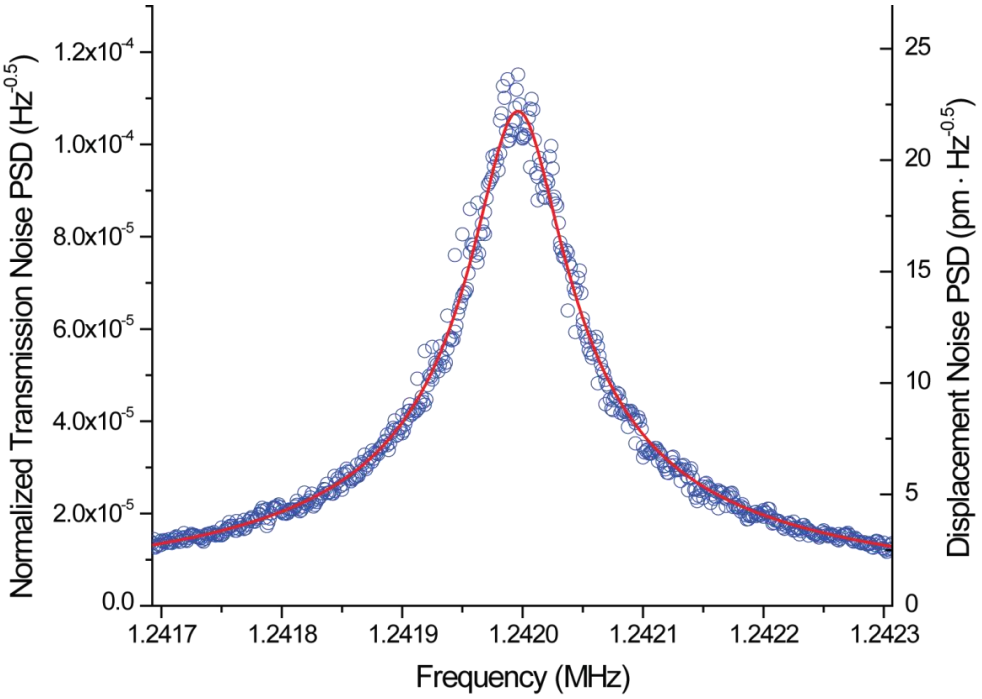

Supplementary Figure S5. The measured normalized transmission noise PSD from the signal channel and the expected displacement noise PSD.

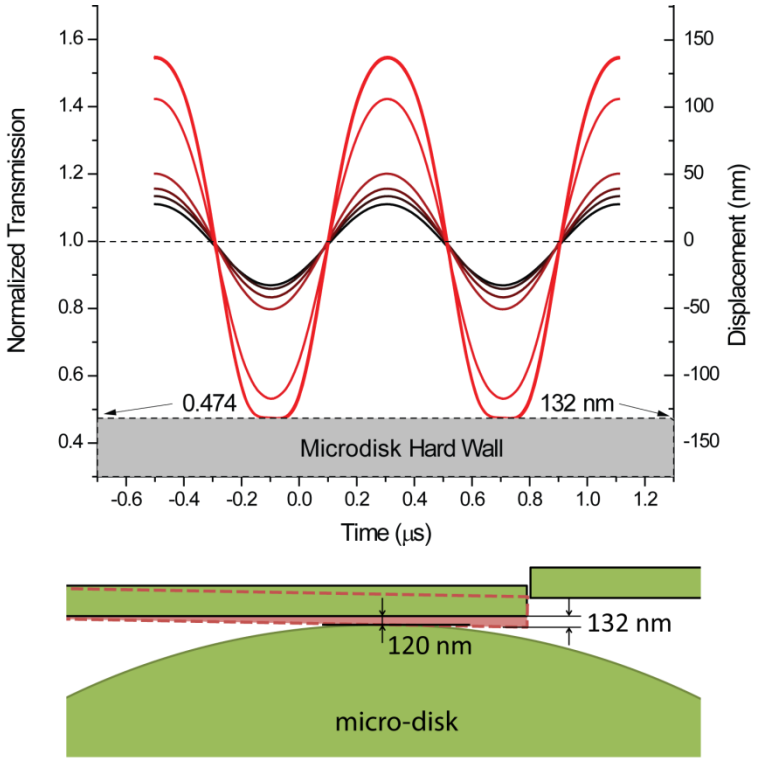

Supplementary Figure S6. Time-domain traces of the transmitted signal in the signal waveguide with increasing vibration amplitude. The waveguide eventually hit the micro-disk and the amplitude is limited by the 120 nm sized gap, as indicated by the flattened bottom in the trace. The maximal displacement at the tip of the cantilever is determined to be 132 nm as an additional calibration to the displacement measurement.

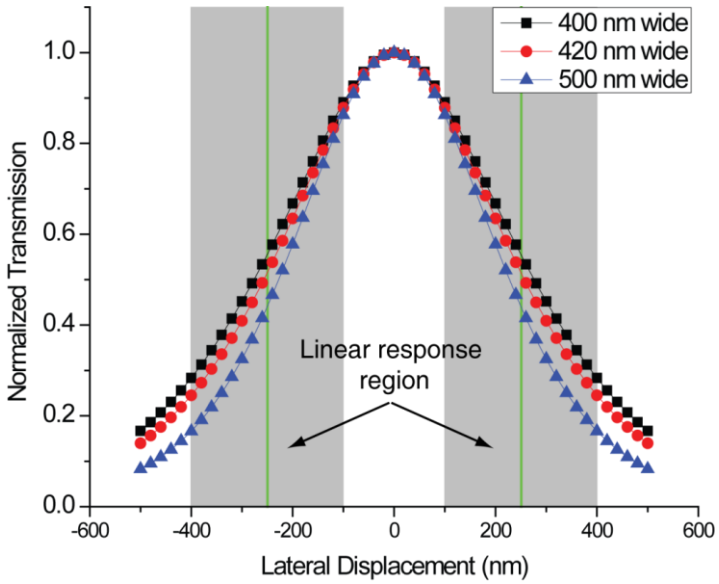

Supplementary Figure S7. FDTD simulation results for the cantilevered signal waveguide design. For each waveguide width, the maximum transmission was normalized to 1 for convenient comparison. The green vertical lines indicate the 250 nm and -250 nm displacement and the shaded areas in the background shows the approximately linear transduction regime for the 400 nm and 420 nm cases.

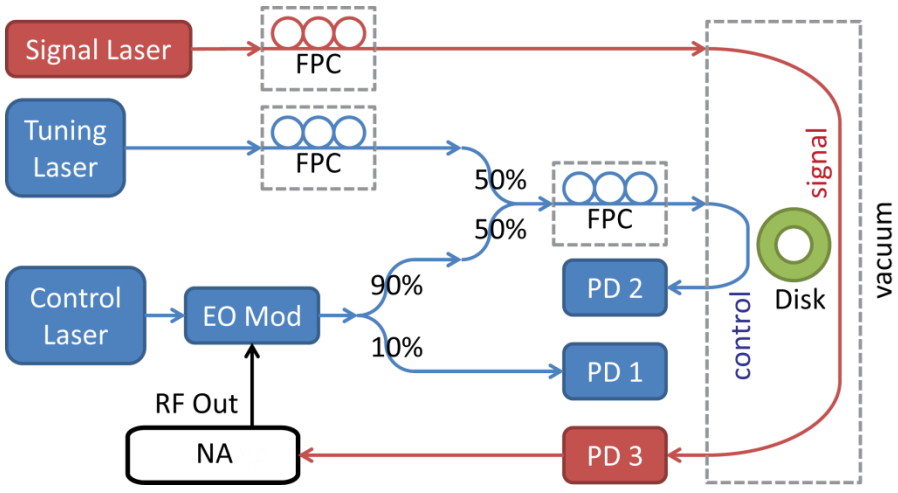

Supplementary Figure S8. Schematic of the measurement setup.

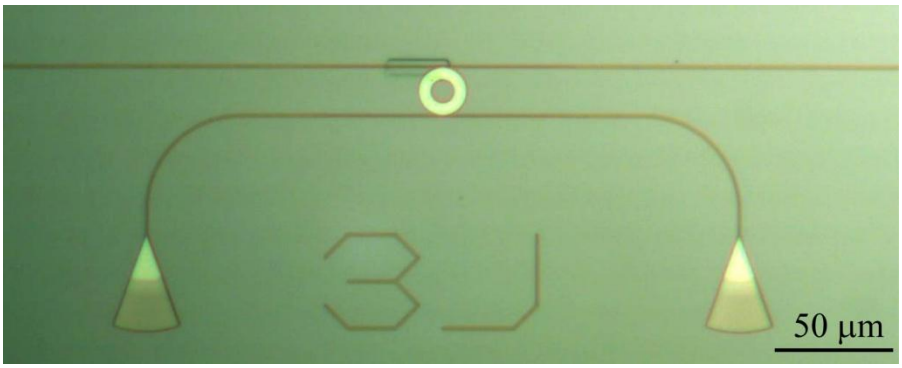

Supplementary Figure S9. Optical microscope image of the device measured in the experiment. There are four grating couplers (two are shown) integrated with the control (bottom) waveguide and the signal (top) waveguide.

Supplementary Tables

Supplementary Table S1. Parameters used to calculate the theoretical values plotted in the figures of the main text.

Symbol	Parameter	Value	Source
ω	Optical frequency	$2\pi\times1.94\times10^{14}$ Hz	Experiment
ω_c	Optical resonance frequency	$2\pi\times1.94\times10^{14}$ Hz	Experiment
g_0	Optomechanical coupling coefficient	$2\pi\times11.3$ MHz/nm	Experiment
Q	Optical quality factor	5×10^4	Experiment
γ	Optical damping rate ($=\omega_c/2Q$)	$2\pi\times1.94\times10^9$ Hz	Experiment
γ_1	Waveguide coupling rate ($=\gamma/2$ for critical coupling)	$2\pi\times9.68\times10^8$ Hz	Experiment
α	Evanescent field decay constant	1/95 nm^{-1}	Simulation
m_{eff}	Effective modal mass (=0.24×cantilever mass)	1.14 pg	Device fabrication

Supplementary Table S2. Optomechanical coupling coefficients (*g* factor), determined by experimental calibration and numerical simulation, and mode volume of different modes

Mode profile $\left\|\vec{E}\cdot\hat{r}\right\|^2$	Mode number (p, m)	$g_{\mathrm{exp}}/2\pi$ (MHz/nm)	$g_{\mathrm{theory}}/2\pi$ (MHz/nm)	V_{mode} ($\mu\mathrm{m}^3$)
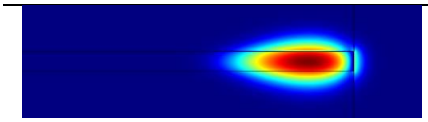	(1,105)	2.30	1.40	39.5
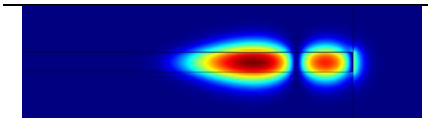	(2,99)	N.A.	1.89	47.7
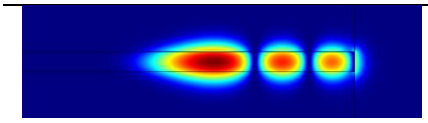	(3,94)	2.15	2.88	57.0
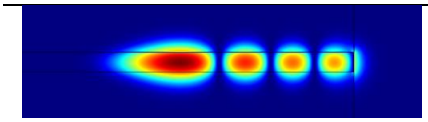	(4,89)	11.3	14.3	65.4
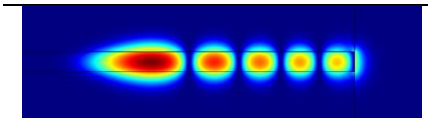	(5,85)	3.39	1.65	74.5

Supplementary Discussion

Theoretical analysis of nonlinear optical force

First, we define the coordinate system of our device as in Supplementary Figure S1. The optical force applied by the cavity on the signal waveguide is given in reference [22]:

$$F_{\mathrm{c}}\ x\ = -\frac{2P_{\mathrm{in}}\gamma_1}{\omega}\frac{g\ x}{\Delta(x)^2+\gamma^2} \tag{S1}$$

Here, the positive of *x*-axis is in the direction pointing away from the micro-disk. $\Delta(x)=\omega-\omega_{\mathrm{c}}(x)$ is the laser (frequency ω) detuning relative to the cavity resonance frequency $\omega_{\mathrm{c}}(x)$ which is dependent on the position of the signal waveguide, $\gamma=\gamma_1+\gamma_2+\gamma_i$ is the total amplitude damping rate of the intra-cavity field including waveguide coupling rate γ_1 (for control waveguide), γ_2 (for signal waveguide) and intrinsic damping rate γ_i. Light is coupled to the cavity through the control waveguide, which is not moving. Here we are only concerned with the optical force on the cantilevered signal waveguide and its induced mechanical motion. One important parameter is the $g(x)=\partial\omega_{\mathrm{c}}/\partial x$ factor which is the optomechanical coupling coefficient between the movable signal waveguide and the micro-disk cavity. Note here both $g(x)$ and the detuning $\Delta(x)=\omega-\omega_{\mathrm{c}}(x)$ are dependent on the signal waveguide's position *x*. We note that the coupling rate γ_2 of the signal waveguide is also dependent of position *x*. However, in our device $\gamma_2 \ll \gamma_1$ so the optomechanical effect on the cavity damping is weak and neglected in the following analysis.

When the signal waveguide moves from its original position x_0 to an arbitrary position *x*, the corresponding new detuning $\Delta(x)$ can be expressed as:

$$\begin{aligned}\Delta(x)&=\omega-\omega_{\mathrm{c}}(x)=\omega-\left[\omega_{\mathrm{c}}(x_0)+\int_{x_0}^{x}\frac{\partial\omega_c}{\partial x'}dx'\right]\\&=\omega-\omega_{\mathrm{c}}(x_0)-\int_{x_0}^{x}g(x')dx'=\Delta_0-\int_{x_0}^{x}g(x')dx'\end{aligned} \tag{S2}$$

Here Δ_0 is the static detuning value when the waveguide is not moved. Using the perturbation treatment employed in reference [20], the optomechanical coupling coefficient, to the first order, has an exponential dependence on the signal waveguide's position:

$$g(x) = g(0)e^{-2\alpha x} = g(x_0)e^{-2\alpha(x-x_0)} = g_0 e^{-2\alpha(x-x_0)} \tag{S3}$$

where α is the field amplitude decay constant outside the rim of the micro-disk and $g_0 = g(x_0)$ is the static value of the optomechanical coupling coefficient when the waveguide is not moved.

Thus, equation (S2) can be written as:

$$\Delta(x) = \Delta_0 - \int_{x_0}^{x} g_0 e^{-2\alpha(x'-x_0)} dx' = \Delta_0 - \frac{g_0}{2\alpha}\left[1 - e^{-2\alpha(x-x_0)}\right] \tag{S4}$$

Then substituting equation (S3) and (S4) into equation (S1), the optical force can be expressed as:

$$F_c(x) = -\frac{2P_{in}\gamma_1}{\omega} \frac{g_0 e^{-2\alpha\delta x}}{\left[\Delta_0 - g_0(1-e^{-2\alpha\delta x})/2\alpha\right]^2 + \gamma^2} = -\frac{2P_{in}\gamma_1}{\omega\gamma} \frac{\xi_0 e^{-2\alpha\delta x}}{\left[\delta_0 - \xi_0(1-e^{-2\alpha\delta x})/2\alpha\right]^2 + 1} \tag{S5}$$

Here we define normalized static detuning $\delta_0 = \Delta_0/\gamma$ and normalized static optomechanical coupling coefficient $\xi_0 = g_0/\gamma$, normalized by the half cavity linewidth γ. We can see that the optical force exerted on the waveguide is a nonlinear function of δ_0 and $\delta x = x - x_0$ which is the signal waveguide's displacement. The nonlinear behavior of the optical force can be seen in the plot of F_c versus δx for different values of δ_0 in Supplementary Figure S2, assuming the independently determined values of the parameters listed in Supplementary Table S1.

We then expand equation (S5) at the waveguide's static position $x = x_0$ to the third order of the waveguide displacement as:

$$F_c(x) = F_c(x_0) + k_1\delta x + k_2\delta x^2 + k_3\delta x^3 + O(\delta x^4) \tag{S6}$$

Thus, the coefficient k_1 is the force constant corresponding to the optical spring effect, k_2 and k_3 are the quadratic and cubic nonlinear coefficients, respectively. Their expression can be derived from the Taylor expansion of equation (S5) and written in the form of polynomials of the normalized static detuning δ_0:

$$k_1 = \frac{4P_{in}\gamma_1\xi_0}{\omega\gamma} \frac{\alpha(1+\delta_0^2) - \xi_0\delta_0}{(1+\delta_0^2)^2} \tag{S7}$$

$$k_2 = \frac{P_{\text{in}}\gamma_1\xi_0}{\omega\gamma\ \left(1+\delta_0^2\right)^3}\left[(2\xi_0^2-4\alpha^2)+12\xi_0\alpha\delta_0-(6\xi_0^2+8\alpha^2)\delta_0^2+12\xi_0\alpha\delta_0^3-4\alpha^2\ \delta_0^4\right] \quad \text{(S8)}$$

$$k_3 = \frac{P_{\text{in}}\gamma_1\xi_0}{\omega\gamma\ \left(1+\delta_0^2\right)^4}\left[\begin{array}{l}\left(-8\xi_0^2\alpha+\frac{8}{3}\alpha^3\right)+\left(8\xi_0^3-\frac{56}{3}\xi_0\alpha^2\right)\delta_0+(16\xi_0^2\alpha+8\alpha^3)\delta_0^2 \\ -\left(8\xi_0^3+\frac{112}{3}\xi_0\alpha^2\right)\delta_0^3+(24\xi_0^2\alpha+8\alpha^3)\delta_0^4-\frac{56}{3}\xi_0\alpha^2\delta_0^5+\frac{8}{3}\alpha^3\delta_0^6\end{array}\right] \quad \text{(S9)}$$

In Supplementary Figure S3a and b, we plot the static optical force $F_{\text{c}}(x_0)$ and the optical spring constant k_1 versus normalized static detuning δ_0 for our device using independently determined parameters listed in Supplementary Table S1.

Theoretical analysis of tunable Duffing nonlinearity

The cantilever waveguide can be modeled as a nonlinear oscillator driven by the optical force with quadratic and cubic nonlinearities. Its equation of motion is that of a typical Duffing oscillator:

$$\frac{d^2(\delta x)}{dt^2}+\mu\frac{d(\delta x)}{dt}+\omega_{\text{m}}^2\,\delta x+\alpha_2\delta x^2+\alpha_3\delta x^3=\frac{f(t)}{m_{\text{eff}}} \quad \text{(S10)}$$

Here m_{eff} is the effective modal mass of the cantilevered signal waveguide; $\mu=\omega_{\text{m}}/Q_{\text{m}}$ is the mechanical damping coefficient; $f(t)$ is the harmonic time-varying driving force generated by the modulated optical power; $\omega_{\text{m}}^2=\omega_{\text{m0}}^2-k_1/m_{\text{eff}}$ is the modified mechanical resonance frequency taking into account the optical spring constant k_1. α_2 and α_3 are the quadratic and cubic nonlinear coefficients. They are given by:

$$\alpha_2=-\frac{k_2}{m_{\text{eff}}}\ ,\ \alpha_3=-\frac{k_3}{m_{\text{eff}}} \quad \text{(S11)}$$

In our system, the nonlinear coefficients α_2 and α_3 are dominated by the optomechanically induced nonlinearity instead of the intrinsic mechanical nonlinearity, because the vibration amplitude of our device is limited to less than 132 nm, which is much less than the critical amplitude (~1 μm) of the device's intrinsic mechanical nonlinearity. The calculated results of α_2 and α_3 of our device are shown in Supplementary Figure S4a and b using equations (S8), (S9) and (S11) with independently determined parameters as listed in Supplementary Table

S1. The same calculated result of α_3 is plotted with the experimental results in Figure 3c of the main text.

The nonlinear effect due to the quadratic term induces sub-harmonic and super-harmonic resonances. But to the primary resonances, the main effect of the quadratic term is a modification to the effective Duffing coefficient in the oscillator's frequency response curve as[30]:

$$\alpha = \alpha_3 - 10\alpha_2^2 / \omega_{\mathrm{m}}^2 \tag{S12}$$

However, in our device and with the conditions used in the measurement, the modification term $10\alpha_2^2 / 9\omega_{\mathrm{m}}^{-2}$ is orders of magnitude smaller than the value of α_3(compare Supplementary Figure S4a and b), except for at the static detuning value when α_3 vanishes. The result is a minor shift of the detuning value for zero nonlinearity, which is below our measurement uncertainty and thus cannot be discerned in our experiment. Therefore we neglect the effect of quadratic nonlinear term in our analysis and omit the subscript 3 of α_3 for conciseness.

Duffing equation of nonlinear oscillators has been analyzed with the method of multiple scales[30]. The amplitude-frequency response curve of a Duffing oscillator can be expressed in an implicit form:

$$\left[\frac{\mu^2}{4} + \left(\sigma - \frac{3\alpha}{8\omega_{\mathrm{m}}} a^2\right)^2\right] a^2 = \frac{f^2}{4m^2\omega_{\mathrm{m}}^2} \tag{S13}$$

Here $\sigma = (\omega - \omega_{\mathrm{m}}) / \omega_{\mathrm{m}}$ is the normalized detuning of the harmonic driving force frequency ω to the modified mechanical resonance frequency ω_{m}. With the increasing driving force, the resonance amplitude increases but leans towards higher or lower frequency side depending on the sign of α, as shown in the experimental results shown in Figure 3a and b of the main text.

The peak amplitude and the frequency at which the peak amplitude is reached have a simple relation:

$$\sigma_{\mathrm{peak}} = \frac{3\alpha}{8\omega_{\mathrm{m}}} a_{\mathrm{peak}}^2 \tag{S14}$$

This relation between σ_{peak} and a_{peak} is called the "backbone" curve. To experimentally determine the cubic nonlinear coefficient α and its relation to the laser static detuning, we

measure the amplitude-frequency response of the device at each laser static detuning value, with increasing modulated control laser power (in at least five steps) to increase the vibration amplitude, as shown in Figure 3a and b of the main text. We then find the peak amplitude a_{peak} and the corresponding detuning σ_{peak}, and fit the result with the backbone curve as given by equation (S14). The standard error given by the fitting result is used as the uncertainty and plotted as error bars in Figure 3c and d.

Supplementary Methods

Method used to calibrate of displacement measurement

The displacement measurement in this paper consistently refers to the lateral (or in-plane) displacement of the free end of the cantilevered signal waveguide. For clarity, in this section, the signal channel transmission and its noise power spectral density (PSD) are always normalized to the transmission value when the waveguide is not displaced. We define signal channel responsivity as the ratio between the change of the normalized transmission and the waveguide's lateral displacement:

$$\Re = \frac{1}{T_0}\frac{\partial T}{\partial x} \tag{S15}$$

We calibrate the responsivity with two methods independently and the results agree well. The first method was the widely employed thermomechanical noise measurement. With no laser sent into the control channel, the signal laser at constant power level and arbitrary off-resonance wavelength was sent into the signal channel. The noise PSD of the transmitted signal laser was measured with a photodetector and a spectrum analyzer. Supplementary Figure S5 shows the normalized noise PSD near the resonance frequency of the cantilever, with a signal laser wavelength of 1555.75 nm. On resonance, the displacement noise PSD of the cantilever is expected to be $S_z = (4k_B T Q_m)/(k\omega_{m0})$, where k_B is the Boltzmann constant, $T = 300\text{K}$ is the absolute temperature in the lab, $Q_m = 1.6\times10^4$ is the mechanical quality factor, $\omega_{m0} = 2\pi\times(1.242\text{MHz})$ is the angular mechanical resonance frequency and $k = 6.94\times10^{-2}\,\text{N}\cdot\text{m}^{-1}$ is the point load spring constant. Q_m and ω_{m0} are obtained by fitting the noise PSD shown in Supplementary Figure S5 with a Lorentzian peak, while *k* is calculated using the standard equation of a cantilever. The expected peak displacement noise PSD $S_z = 4.92\times10^{-22}\ \text{m}^2\cdot\text{Hz}^{-1}$ corresponds to the measured peak normalized transmission noise PSD $P_{max}^{norm} = 1.15\times10^{-8}\ \text{Hz}^{-1}$ obtained from Supplementary Figure S5. Therefore the responsivity is calibrated to be $\Re = (P_{max}^{norm}/S_z)^{0.5} = 4.83\ \mu\text{m}^{-1}$.

The maximal displacement that the signal waveguide can reach is limited by the 120 nm sized gap between the waveguide and the micro-disk. This provides the second method to

independently calibrate the displacement measurement at the large amplitude regime. Determined from the geometry of the device and the mode profile of the cantilever resonance, the maximal displacement of the tip of the cantilevered waveguide is 132 nm, as is illustrated in Supplementary Figure S6. The strong optical force applied by the micro-disk cavity on the signal waveguide is sufficient to drive the signal waveguide to reach this maximal amplitude and be stopped by the micro-disk. Supplementary Figure S6 shows the time-domain signal measured with increasing vibration amplitude. At high amplitude, the sinusoidal waveform shows a flattened bottom, indicating that the waveguide is hitting the side wall of the micro-disk. Thus, the transmission value at the flattened amplitude is 0.474, corresponding to a displacement of 132 nm at the tip of the cantilevered waveguide. Hence the responsivity is evaluated to be $\Re = (1-0.474)/(132\text{nm}) = 3.98\ \mu\text{m}^{-1}$. The discrepancy with the value calibrated with thermomechanical noise measurement method is due to the nonlinear response of the waveguide transmission at high amplitude, as explained in the Supplementary Discussion. It is interesting to note that there is no pull-in effect like that in electrostatic-ly actuated MEMS devices because optical force decreases when the waveguide touches the micro-disk, due to the reduction of the optical *Q* and strong coupling. The mechanical spring of the waveguide is also large enough so that it will not stick to the micro-disk due to surface forces.

Cantilevered signal waveguide design

The signal waveguide is designed with a gap between the free end of the cantilevered section and the receiving end of the fixed section. In addition, to detect the cantilever waveguide's lateral (or in-plane) motion, a lateral offset between the waveguide ends is also needed. The transmission through the cantilevered signal waveguide has been numerically analyzed with Finite Difference Time Domain (FDTD) simulations, which is a rigorous treatment that takes into account the mode evolution during the propagation through the gap, the coupling from the gap back to the receiving waveguide and all the reflections that occur in this process. We studied three different cases: 400 nm, 420 nm and 500 nm wide waveguides. The simulation results are shown in Supplementary Figure S7, suggesting that 500 nm wide waveguide has the steepest slope on both sides of the curve and 400 nm wide the least steep. 420 nm wide waveguide was eventually chosen based on various considerations, especially the trade-off between a softer cantilever and more sensitive transduction. In order to achieve the most linear transduction in a large

displacement range, we designed the initial lateral offset to be 250 nm, which is almost in the center of the linear part of the transmission curves (shaded areas in Supplementary Figure S7). In the actual device, the displacement was limited by the fixed gap between the cantilever and the disk resonator hence never exceeded 132 nm towards the disk and 140 nm away from the disk (see Supplementary Figure S6), so the cantilevered signal waveguide remains in the approximately linear transduction regime even when being driven to the highest amplitude. Nevertheless, the imperfection in the linearity still leads to the discrepancy between the values of responsivity calibrated by the two methods described in Section 3. The receiving waveguide is designed to be farther away from the disk than the cantilever, so the transmission increases (decreases) when the cantilever moves away from (towards) the disk.

Experimental calibration of *g* factor

The optomechanical coupling coefficient or the *g* factor is one of the most important parameters of cavity optomechanical systems. We experimentally determine the *g* factor by measuring the thermomechanical noise of the device using the "slope detection" method. In the experiment, a probing laser at constant power is sent into the control channel and tuned on the slope of the resonance dip in the transmission spectrum (see Figure 1c in the main text). The thermomechanical vibration of the cantilever dispersively perturbs the disk resonance introducing amplitude noise in the transmitted probing laser power, which was measured by a photodetector and a spectrum analyzer. The *g* factor can be determined experimentally using the following equation:

$$|g| = \left|\frac{\partial \omega_c}{\partial x}\right| = \left(\frac{2\pi c}{\lambda_{Prob}^2}\right)\left|\frac{dT}{d\lambda}\right|_{\lambda_{Prob}}\Bigg|^{-1} \frac{\sqrt{S_v/S_z}}{P_{Prob}G} \tag{S16}$$

where S_v is the measured voltage noise power spectral density (PSD), S_z is the expected cantilever displacement noise PSD which is described in Section 3, P_{Prob} is the probing laser power, G (in V/W) is the transduction gain factor of the photodetector, c is the light velocity in vacuum, λ_{Prob} is the probing laser wavelength, $T(\lambda)$ is the measured transmission spectrum of the resonance through the control channel, including the input and output grating couplers, its derivative with respect to λ ($dT/d\lambda$) is estimated by linear curve fitting near the probing laser

wavelength. The experimentally determined values of the *g* factor are listed in Supplementary Table S2 for the modes labeled in Figure 1c of the main text.

Theoretical calculation of g factor

In order to theoretically calculate the optomechanical coupling coefficient, or the *g* factor, we first used Finite-Element-Method (FEM) to calculate the Whispering Gallery Mode (WGM) profiles $\vec{E}(\vec{r})$ of the disk resonator without control or signal waveguide, so that we could take advantage of the axisymmetry of the disk resonator to simplify the large scale 3D problem into a 2D problem[24]. Subsequently we employed a perturbation treatment derived from energy considerations[44] to take into account the resonance frequency shift induced by the existence of the nearby waveguide and its motion:

$$\frac{\Delta\omega_c'(\delta x)}{\omega_c'} = -\frac{1}{2}\frac{\iiint_{V_{\mathrm{Cant}}(\delta x)} \varepsilon(\vec{r})-1 \left|\vec{E}(\vec{r})\right|^2 d^3\vec{r}}{\iiint_V \varepsilon(\vec{r})\left|\vec{E}(\vec{r})\right|^2 d^3\vec{r}} \tag{S17}$$

where $\varepsilon(\vec{r})$ is the dielectric constant, ω_c' is the resonance frequency without waveguides nearby, $\Delta\omega_c'(\delta x)$ is the resonance frequency shift with respect to ω_c' when the cantilever displacement is δx, $V_{\mathrm{Cant}}(\delta x)$ is the volume of the cantilever when the cantilever displacement is δx and V is the entire space. The *g* factor when the cantilever is at its original position can be derived as:

$$g = \left.\frac{d(\Delta\omega_c')}{d(\delta x)}\right|_{\delta x=0} \tag{S18}$$

In equation (S17), ω_c' was solved in the FEM simulation and the integrals on the right hand side were calculated numerically from the simulation results. The derivative in equation (S18) was also calculated numerically by five point method. The calculation results agree reasonably well with the experimentally calibrated *g* factors, as listed in Supplementary Table S2.

Mode volume is another important characteristic of resonance modes. It is defined as[24]

$$V_{\mathrm{mode}} = \frac{\iiint_V \varepsilon(\vec{r})\left|\vec{E}(\vec{r})\right|^2 d^3\vec{r}}{\max\left[\varepsilon(\vec{r})\left|\vec{E}(\vec{r})\right|^2\right]} \tag{S19}$$

where max[···] denotes the maximum value of its functional argument. The numerically calculated mode volumes are also included in Supplementary Table S2. We note that the TE mode (4,89), which our experiment focuses on, has a particularly high g factor because of the good phase-matching with the waveguide mode.

Supplementary Reference

44 Johnson, S. G. *et al.* Perturbation theory for Maxwell's equations with shifting material boundaries. *Physical Review E* **65**, 066611 (2002).